

Enhancement of Spin–Orbit Torque by Strain Engineering in SrRuO₃ Films

Jinwu Wei, Hai Zhong, Jiuzhao Liu, Xiao Wang, Fanqi Meng, Hongjun Xu, Yizhou Liu, Xin Luo, Qinghua Zhang, Yao Guang, Jiafeng Feng, Jia Zhang, Lihong Yang, Chen Ge,* Lin Gu, Kuijuan Jin, Guoqiang Yu,* and Xiufeng Han

Complex oxides with 4d/5d transition metal ions, e.g., SrRuO₃, usually possess strong spin–orbit coupling, which potentially leads to efficient charge-spin interconversion. As the electrical transport property of SrRuO₃ can be readily tuned via structure control, it serves as a platform for studying the manipulation of charge-spin interconversion. Here, a factor of twenty enhancement of spin–orbit torque (SOT) efficiency via strain engineering in a SrRuO₃/Ni₈₁Fe₁₉ bilayer is reported. The results show that an orthorhombic SrRuO₃ leads to a higher SOT efficiency than the tetragonal one. By changing the strain from compressive to tensile in the orthorhombic SrRuO₃, the SOT efficiency can be increased from an average value of 0.04 to 0.89, corresponding to a change of spin Hall conductivity from 27 to 441 × \hbar/e (S cm⁻¹). The first-principles calculations show that the intrinsic Berry curvature can give rise to a large spin Hall conductivity (SHC) via the strain control, which is consistent with the experimental observations. The results provide a route to further enhance the SOT efficiency in complex oxide-based heterostructures, which will potentially promote the application of complex oxides in energy-efficient spintronic devices.

1. Introduction

Current-induced spin–orbit torques (SOTs) in the materials with strong spin–orbit coupling (SOC) continuously attract attention due to their promising prospect in energy-efficient and ultrafast spintronic devices.^[1–4] Exploration of the new mechanism for enhancing the SOT efficiency and development of new SOT materials are crucial for practical applications. Recently, the conducting perovskite oxides with 4d/5d transition metal ions are predicted to have large SOT

efficiency due to the strong spin Hall conductivity (SHC) σ_{SH} that arises from the competition between crystal field energy and large SOC of conduction electrons.^[5–10] The ruthenate conductors are of particular interests because they have shown many appealing features due to the strong SOC originated from the Ru ion,^[11–14] such as the superconducting property in Sr₂RuO₄,^[15] the strong magnetocrystalline anisotropy of SrRuO₃ (SRO) at low temperature,^[16] and the topological Hall effect.^[17] Recently, the spin-charge conversion has also been experimentally reported through spin pumping experiments in the SrRuO₃/La_{0.7}Sr_{0.3}MnO₃ and SrRuO₃/YIG heterostructures.^[18,19] Moreover, it was found that a current can generate a damping-like SOT in the SRO at room temperature, and a corresponding intrinsic SHC of $\sigma_{\text{SH}} \geq 200 \times \hbar/e$ (S cm⁻¹)

was obtained.^[20] The large room-temperature SHC establishes SRO as a potential candidate material for generating SOT in the spintronic devices.

One intriguing property of SRO lies in the interplay between its transport property and crystal structure. The theories and experiments have demonstrated that the structure of SRO films can be controlled by using different substrates.^[21–25] The SRO grown on orthorhombic substrates, such as (110) DyScO₃, GdScO₃, and NdGaO₃, exhibits a tetragonal structure.^[21,22] By contrast, the SRO exhibits an orthorhombic structure when

Dr. J. Wei, Dr. H. Zhong, Dr. X. Wang, Dr. F. Meng, Dr. H. Xu, Dr. Y. Liu, Dr. X. Luo, Dr. Q. Zhang, Dr. Y. Guang, Prof. J. Feng, Prof. L. Yang, Prof. C. Ge, Prof. L. Gu, Prof. K. Jin, Prof. G. Yu, Prof. X. Han
Beijing National Laboratory for Condensed Matter Physics
Institute of Physics
Chinese Academy of Sciences
Beijing 100190, China
E-mail: gechen@iphy.ac.cn; guoqiangyu@iphy.ac.cn

Dr. J. Wei, Dr. X. Wang, Dr. H. Xu, Dr. Y. Guang, Prof. J. Feng, Prof. G. Yu, Prof. X. Han
Center of Materials Science and Optoelectronics Engineering
University of Chinese Academy of Sciences
Beijing 100049, China

Dr. J. Wei, Dr. H. Xu, Prof. L. Gu, Prof. K. Jin, Prof. G. Yu, Prof. X. Han
Songshan Lake Materials Laboratory
Dongguan, Guangdong 523808, China

Dr. J. Liu, Prof. J. Zhang
School of Physics
Huazhong University of Science and Technology
Wuhan, Hubei 430074, China

Prof. C. Ge, Prof. K. Jin
School of Physical Sciences
University of Chinese Academy of Science
Beijing 100049, China

 The ORCID identification number(s) for the author(s) of this article can be found under <https://doi.org/10.1002/adfm.202100380>.

DOI: 10.1002/adfm.202100380

it is grown on cubic substrates, such as (001) SrTiO₃, LSAT, and KTaO₃.^[23–25] To accommodate the compressive or tensile strains imposed by the substrates, the RuO₆ octahedra need to distort through tilting and rotation.^[23] Consequently, the structure change induced by substrate strain can strongly affect the transport and magnetic properties of SRO films. For instance, the tetragonal SRO on DSO has a higher resistivity than orthorhombic SRO on STO,^[21] and the resistivity of tetragonal SRO under compressive strain is lower than that of the film with tensile strain.^[22] The results can be explained that the strain-induced RuO₆ octahedra distortion modifies the crystal field splitting, which influences the electronic band structures.^[25–27] As the intrinsic spin Berry curvature and SHC are closely related to the band structure in SRO, the spin-charge conversion can likely be manipulated by the strain, which, however, has not been explored.

In this work, we study the SOT efficiency in SRO/Ni₈₁Fe₁₉ (Permalloy, Py) films grown on different substrates, which introduce different structure phases and strains in the SRO films. The SOT efficiency in the orthorhombic SrRuO₃ films can be significantly increased from an average value of 0.04 to 0.89 by changing the strain from compressive to tensile. The first-principles calculations indicate that the large SHC is originated from the intrinsic spin Berry curvature, and the SHC can be efficiently controlled by strain.

2. Results and Discussion

2.1. Sample Structure

The high-quality SRO films were epitaxially grown by pulsed laser deposition (PLD) on single crystal substrates with different lattice constants, including the cubic (001)-oriented KTaO₃ (KTO), SrTiO₃ (STO), (LaAlO₃)_{0.3}(Sr₂TaAlO₆)_{0.7} (LSAT) and orthorhombic (110)-oriented GdScO₃ (GSO), DyScO₃ (DSO), NdGaO₃ (NGO) substrates. The ferromagnetic Py polycrystalline films were then deposited on SRO films by a magnetron sputtering system. A schematic depiction of heteroepitaxial growth of SRO layer on different substrates with the pseudocubic unit cell is shown in **Figure 1a**. The bulk SRO has an orthorhombic phase with lattice parameters $a = 5.5670$ Å, $b = 5.5304$ Å, and $c = 7.8446$ Å, which can also be represented as a pseudocubic structure with $a = 3.93$ Å. All the substrates in this work are regarded as pseudocubic structure. The lattice constants are shown in **Figure 1b**. The strain applied in SRO films varies from compressive strain -1.91% on NGO, -1.57% on LSAT, and -0.64% on STO to tensile strain $+0.38\%$ on DSO, $+0.89\%$ on GSO, and $+1.5\%$ on KTO. Because of the lattice mismatch between the films and substrates, the SRO lattices can be stretched or compressed, which alters the tilting and rotation angle of the RuO₆ octahedra. The scanning transmission electron microscopy (STEM) measurement was performed to verify the quality of the SRO films. **Figure 1c,d** shows the high-angle annular dark-field (HAADF) images of the SRO/Py bilayers grown on the (001) STO and (001) KTO substrates, respectively. The SRO films have a high-quality epitaxial structure, and the interfaces between the films and substrates are sharp. The adjacent Py films are also distinct and not oxidized

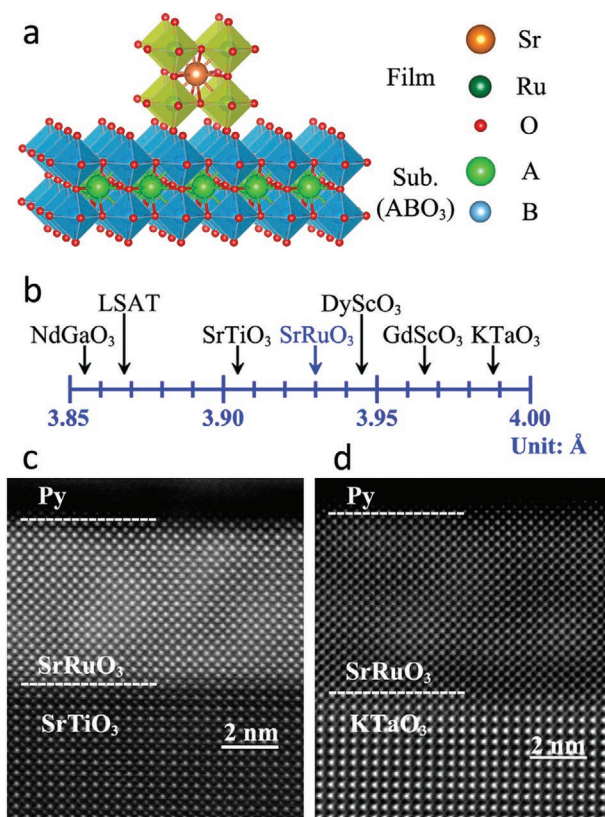


Figure 1. Sample structure. a) Schematic of the SRO film grown on the substrate. Both the film and substrate can be considered as the pseudocubic phase with the unit cell of RuO₆ octahedra. The [001] direction of the octahedra is perpendicular to the SRO film. b) The lattice parameters of the SRO film and different substrates. The NGO, LSAT, and STO exert compressive strain to the SRO films, and the DSO, GSO, and KTO exert tensile strain. c,d) STEM images of the SRO films on the STO and KTO substrates, showing the clearly layered structures and atomically sharp interface.

at the interface (see section S1 of Supporting Information). The structure phases of the SRO films were characterized by X-ray reciprocal space mapping (RSM) (see section S2 of Supporting Information). The RSM results suggest that the SRO films grown on the (110) orthorhombic substrate have a tetragonal structure and the SRO films grown on the cubic substrate have an orthorhombic phase, which is consistent with the previous work.^[21–24]

2.2. Extraction of SOT Efficiency

The current-induced SOT efficiency is evaluated by the spin-torque ferromagnetic resonance (ST-FMR) technique,^[28–31] as shown in **Figure 2a**. All the measurements were performed at room temperature. **Figure 2b,d** shows the typical ST-FMR spectra for the SRO/Py on NGO and KTO substrates. The ST-FMR spectrum can be analyzed by the equation $V_{\text{mix}} = V_s F_s(H_{\text{ext}}) + V_a F_a(H_{\text{ext}})$, which consists of the Lorentz symmetric and antisymmetric components (see section S3 of Supporting Information). In terms of the ST-FMR model,^[32–34] the symmetric component V_s is mainly attributed to the damping-like

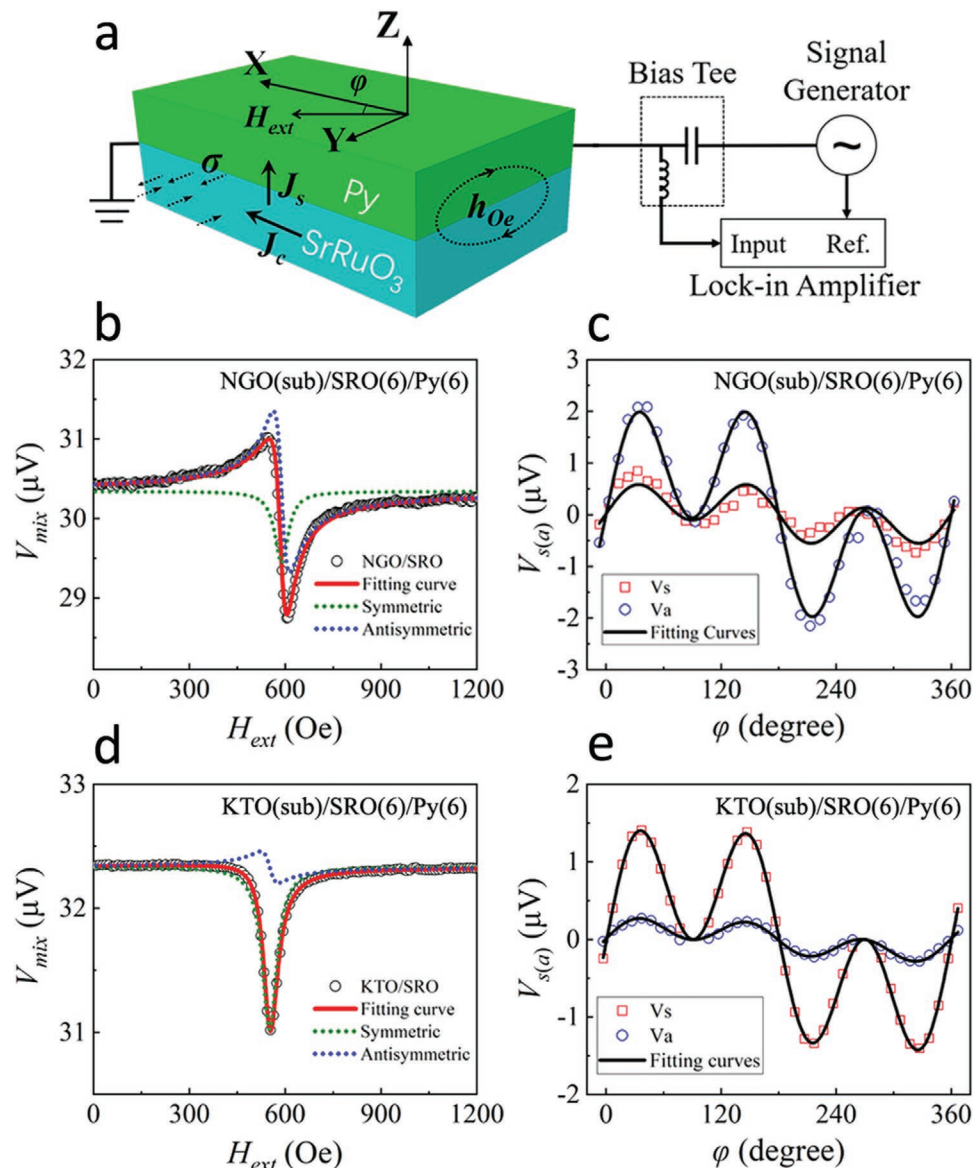


Figure 2. ST-FMR measurement. a) The schematic of ST-FMR measurement. A radio frequency charge current J_c with a frequency of 6 GHz and power of 13 dBm from the signal generator is applied to the device, which induces an alternating spin current J_s due to the spin Hall effect. The spin current then flows into the adjacent Py layer with the polarization direction σ and exerts a torque on the magnetization. The mixing voltage is measured by using lock-in amplifier. b,d) ST-FMR spectra of the SRO (6 nm)/Py (6 nm) bilayers on the NGO and KTO substrates, respectively. The external magnetic field is oriented at $\varphi = -45^\circ$ with respect to the charge current direction. Black circles denote the measured data. Red solid lines are the fitting curves, which are composed of the symmetric (green dashed) and antisymmetric (blue dashed) components. c,e) Angular dependence of V_s and V_a of the SRO (6 nm)/Py (6 nm) bilayers on NGO and KTO substrates, respectively. The black lines are the fitting curves by using the relationship of $\cos\varphi\sin 2\varphi$.

(DL) torque, while the antisymmetric component V_a is originated from the field-like (FL) torque and Oersted field. From the ratio of the symmetric (V_s) and antisymmetric (V_a) components, one can define the SOT efficiency^[33]

$$\xi_{\text{SOT}} = \frac{V_s}{V_a} \frac{e}{\hbar} \mu_0 M_0 t_{\text{FM}} t_{\text{SRO}} \sqrt{1 + \frac{4\pi M_{\text{eff}}}{H_r}} \quad (1)$$

Here, e is the electron charge, \hbar is the reduced Planck constant, $\mu_0 M_0$ is the saturation magnetization of Py layer, t_{FM} is the thickness of Py, t_{SRO} is the thickness of SRO, $4\pi M_{\text{eff}}$ is the

effective magnetization of Py layer, and H_r is the resonance field, respectively. We note that the FL torque is much weaker than the torque arising from the Oersted field, and hence the SOT efficiency is approximately equal to the DL torque efficiency (ξ_{DL}), i.e., $\xi_{\text{SOT}} \approx \xi_{\text{DL}}$ (see section S4 of Supporting Information). The ST-FMR spectra show that the symmetric component is larger than the antisymmetric one for the sample grown on the KTO substrate, while the symmetric component is smaller for the sample grown on the NGO substrate. As the symmetric component corresponds to the DL torque efficiency, the direct comparison implies that the SRO grown on KTO

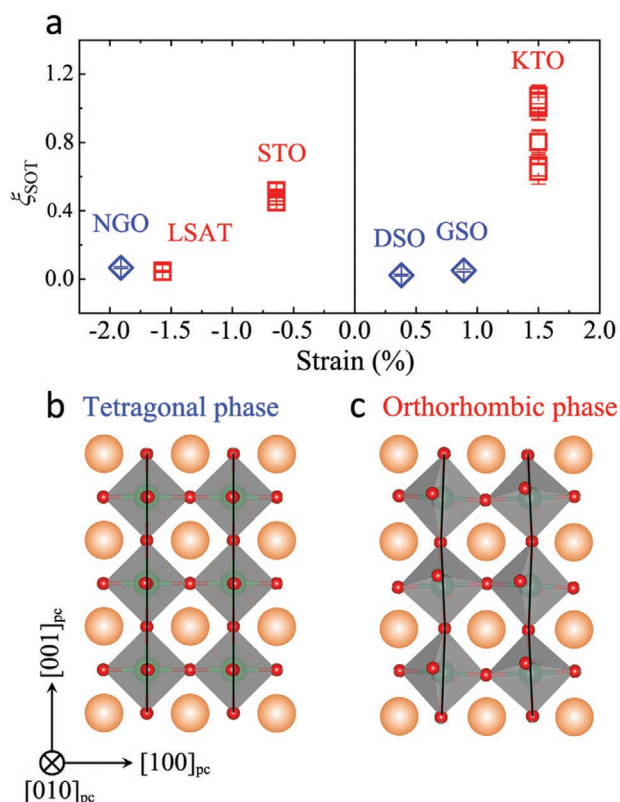


Figure 3. SOT efficiencies of SRO on different substrates. a) The SOT efficiencies of SRO/Py bilayers on various substrates. To ensure the observed large SOT efficiency for the KTO substrate is repeatable, we performed the SOT characterization for many devices using SRO films from different batches, the structure of which may be slightly different. Blue hollow rhombus represents the (110) orthorhombic substrates. Red hollow square represents the (001) cubic substrates. b,c) Schematic of the tetragonal phase and orthorhombic phase. The out-of-plane direction is aligned with the [001] direction of the pseudocubic phase.

substrate leads to a larger DL torque efficiency compared to the NGO substrate. Figure 2c,e shows the angular dependences of $V_{\text{s(a)}}$ for the samples on NGO and KTO substrates, which can be nicely fitted by the angular relationship of $\cos\varphi\sin2\varphi$.^[35,36] Based on the fitting, the V_{s} and V_{a} can be accurately extracted, and hence the current-induced SOT efficiency ξ_{SOT} is further evaluated by Equation (1). Note that there is a parasitic voltage with the same angular relationship of $\cos\varphi\sin2\varphi$ arising from the inverse spin Hall effect due to the spin pumping, which is much smaller than the ST-FMR voltage and has been neglected here (see section S5 of Supporting Information).

2.3. Comparison of the SOT Efficiencies for Different Substrates

Figure 3a summarizes the SOT efficiencies of the SRO films on different substrates. To get reliable results, the SOT efficiencies for each structure are characterized for at least five devices. The first important feature is that the SOT efficiencies of samples on cubic substrates (LSAT, STO, KTO) are larger than that on orthorhombic substrates (NGO, DSO, GSO). As shown by the RSM results (see section S2 of Supporting Information), the

SRO films grown on the (110) orthorhombic substrate have a tetragonal phase, as shown in Figure 3b. Whereas the SRO films grown on the cubic substrate have an orthorhombic phase, as shown in Figure 3c. This result implies that the SOT efficiency is closely related to the structure of SRO. For the tetragonal SRO structure, the RuO_6 octahedra are rotated only about the [001] direction (pseudocubic structure). The orthorhombic SRO is a three-tilt system, where the RuO_6 octahedra are not only rotated about the [001] direction but also tilted about the [100] and [010] directions. From the viewpoint of crystal symmetry, the orthorhombic phase has a larger spin Berry curvature and thereby a larger SHC than the tetragonal phase due to the band overlaps and crossings induced by the octahedra distortion.^[7,37] The previous experimental work showed that the SOT efficiency was correlated to the current flow direction with respect to the crystal orientation in the SrIrO_3 thin film.^[37] However, this phenomenon is not observed in our sample (see section S6 of Supporting Information), which indicates the weak correlation between SOT and crystalline direction and requires further exploration. The second feature shown in Figure 3a is that the SOT efficiencies of orthorhombic SRO films are strongly dependent on the substrate-induced strain. Particularly for the KTO substrate, the tensile strain results in large SOT efficiencies ranging from 0.62 to 1.07 among nine different devices, and the average value for all the measured devices is 0.89. This value is larger than that of heavy metal ($\xi_{\text{DL}} = 0.05\text{--}0.20$ for Pt,^[38–40] $|\xi_{\text{DL}}| = 0.3\text{--}0.55$ for W^[41,42]) and close to that of the topological insulator ($\xi_{\text{DL}} = 2.0\text{--}3.5$ for Bi_2Se_3 ^[29]). When the strain changes from tensile to compressive stress, the ξ_{DL} of SRO decreases with respect to the strain. This result provides a broad control range from 0.04 to 0.89 for the SRO films through the strain engineering, which also covers the previously reported values (e.g., $\xi_{\text{DL}} = 0.3$ for Py/SRO on STO substrate^[18]).

To understand the underlying physics of the strain effect, we first examine the influence of strain on the interfacial spin transparency T_{in} , which can affect the DL torque efficiency. The correlation between T_{in} and ξ_{DL} is $\xi_{\text{DL}} = T_{\text{in}}\theta_{\text{SH}}$. The T_{in} is smaller than unity due to the finite spin-mixing conductance of the interface. θ_{SH} is the spin Hall angle to determine the strength of SHE. The interfacial spin transparency T_{in} can be

determined by^[43,44] $T_{\text{in}} = \frac{2G^{\uparrow\downarrow} \tan h(t_{\text{SRO}}/2\lambda_{\text{sd}})}{1/\lambda_{\text{sd}}\rho_{\text{SRO}} + 2G^{\uparrow\downarrow} \coth h(t_{\text{SRO}}/\lambda_{\text{sd}})}$, where

$G^{\uparrow\downarrow}$ is interfacial spin mixing conductance, ρ_{SRO} is the resistivity, and λ_{sd} is the spin diffusion length. The electrical resistivities of SRO films on different substrates are determined by the four-terminal measuring method (see section S7 of Supporting Information). The SRO films under large tensile strain (SRO on KTO) have higher resistivity compared to the compressively strained SRO films (SRO on STO or LSAT), which suggests that electron correlation in SRO is enhanced due to the lattice distortion induced by tensile strain. We have further estimated the spin diffusion length $\lambda_{\text{sd}} = 1.9\text{--}2.2$ nm based on the results of the SRO thickness dependence of DL torque efficiency (see section S4 of Supporting Information), and the effective interfacial spin mixing conductance $G_{\text{eff}}^{\uparrow\downarrow}$ ranging from 3.06×10^{14} to $3.57 \times 10^{14} \Omega^{-1}\text{m}^{-2}$ based on the NiFe thickness dependence of damping constant (see section S7 of Supporting Information). The interfacial spin transparency T_{in} is thus determined to be

0.82–0.85 for the three samples with orthorhombic SRO. The almost same T_{in} for the samples grown on different substrates indicates that it cannot be responsible for the great change of DL torque efficiency. Therefore, this wide range of ξ_{DL} from 0.04 to 0.89 controlled by misfit strain is mainly attributed to the intrinsic spin Hall effect in SRO films. The SHC of SRO films can be deduced from the $\sigma_{SH} = (\hbar/2e)\xi_{DL}\sigma_{SRO}/T_{in}$. The tensile strain-induced lattice distortion in SRO on KTO leads to a large SHC $\approx 441 \times \hbar/e$ (S cm⁻¹). While under compressive strain, the SRO on STO and LSAT have relatively smaller SHC $\approx 285 \times \hbar/e$ and $27 \times \hbar/e$ (S cm⁻¹), respectively. The large variation of the SHC can likely be explained by the change of the spin Berry curvature, which is determined by the crystal structure and SOC of conduction electrons in SRO.

2.4. Physical Origin of the Enhanced SOT Efficiency

To gain more insight into the strain effect on the SOT efficiency and SHC, we calculate the spin Berry curvature and the intrinsic SHC for SRO with tetragonal and orthorhombic phases by using first-principles calculations, as listed in the section S8 of Supporting Information. The calculation results show that the SHC of the orthorhombic SRO is larger than that of the tetragonal one ($11.3 \times \hbar/e$ (S cm⁻¹)), which is consistent with the first feature of the experimental results. This is also in accord with the previous experimental results,^[37] in which the orthorhombic SrIrO₃ is found to have a larger SHC than the tetragonal one because the orthorhombic phase exhibits narrow t_{2g} electron bands and has more band crossings due to the octahedral rotation and tilting. The recent theoretical work has also demonstrated that the octahedral rotation and tilting in the perovskite oxides can break up the t_{2g} manifold into multiple sub-bands.^[10] Consequently, this enhances the overlaps or mixings of d-orbitals through the SOC interaction, which leads to a larger spin Berry curvature and thereby a larger SHC. On the other hand, the intrinsic SHC for the orthorhombic SRO under different strains are also calculated and shown in Figure 4. The strain is considered by using different lattice parameters, which are given based on the substrate lattices.^[23]

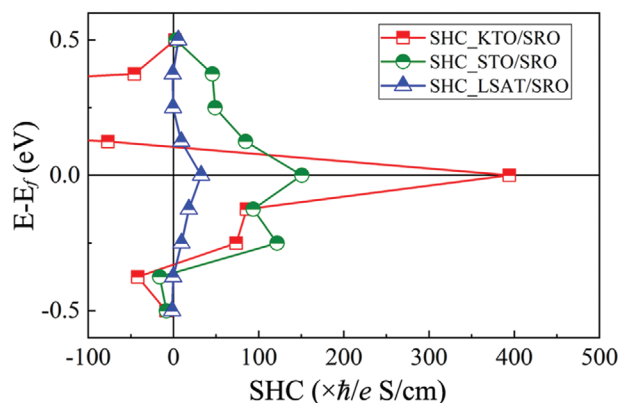


Figure 4. Theoretical spin Hall conductivity of SRO. Energy dependence of spin Hall conductivity obtained from the first-principles calculations for the orthorhombic SRO under different strains, corresponding to the SRO on KTO, STO, and LSAT substrates.

The intrinsic SHC for the SRO on KTO is found to be as large as $400 \times \hbar/e$ (S cm⁻¹) at Fermi energy. With the decrease of the misfit strain, corresponding to the substrates change from KTO to STO and LSAT, the SHC decreases gradually, which is consistent with the second feature of our experimental results. As the band structure is susceptible to the strain in the SRO,^[11] the overlaps or mixings of d-orbitals are likely modified by the strain, and hence the correlated SHC is affected. In fact, the influence of strain on the mixing or overlaps between the d_{xz} and d_{yz} orbitals can be observed in the band structures, as shown in Figure S7 in the Supporting Information. One can note that the calculated SHC of SRO on KTO is slightly lower than the average value of SHC evaluated from our experiments. This may be partially ascribed to the fact that we only consider the intrinsic SHC of perfect crystal structures, while other extrinsic SHC contributions existing in real samples have not been considered in the present calculation. For instance, the SRO films are usually accompanied by oxygen vacancies in the preparation process, which are also important to the transport property of SRO.^[45]

3. Conclusion

We have studied the SOT efficiency in SRO films by strain engineering and obtained a great enhancement of SOT efficiency ranging from an average value of 0.04 to 0.89, corresponding to a change of spin Hall conductivity from 27 to $441 \times \hbar/e$ (S cm⁻¹). The first-principles calculations demonstrated that the enhanced SOT efficiency is dependent on the electronic band structure and spin Berry curvature due to the distortion of RuO₆ octahedral, which are consistent with the experimental results. This work provides a path to manipulate the SOT efficiency of SRO films and will facilitate the potential applications in spintronic devices.

4. Experimental Section

Materials: The SrRuO₃ thin films were epitaxially grown on various substrates by pulsed laser deposition (PLD) using a 308-nm XeCl excimer laser. Various substrates, including NGO, LSAT, STO, DSO, GSO, and KTO, were utilized in order to investigate the strain effect. The laser fluence was ≈ 1.3 J cm⁻² and the laser frequency was 2 Hz. The distance between the target and substrate was ≈ 50 mm. The SrRuO₃ films were deposited at 600 °C in a flowing oxygen atmosphere at the oxygen pressure of 13 Pa. The deposition rate of SrRuO₃ films was calibrated by X-ray Reflection (XRR) using a Rigaku Smartlab instrument. The SrRuO₃ films were transferred to the chamber of magnetron sputtering, and then the chamber was vacuumed. The Py films were sputter deposited at Ar pressure of 0.08 Pa with a background pressure $\approx 1 \times 10^{-6}$ Pa. The capping layers MgO (2 nm)/Ta (2 nm) were added to prevent oxidation of Py films.

Device: The samples were fabricated into a strip with a length of 50 μ m and width of 20 μ m and assembled with a coplanar waveguide (CPW) using standard photolithography and argon ion etching techniques. The Cr(5 nm)/Au(80 nm) bilayers were deposited by magnetron sputtering as the CPW electrodes. The CPW has a signal line with a width of 80 μ m and the gap between the signal line and ground was 40 μ m. In order to avoid the electric leakage of the oxide substrate after the etching process, the samples were annealed at 250 °C for 20 min under an oxygen atmosphere.

Supporting Information

Supporting Information is available from the Wiley Online Library or from the author.

Acknowledgements

This work was supported by the National Key Research and Development Program of China (Grant Nos. 2017YFA0206200 and 2017YFA0303604), the Science Center of the National Science Foundation of China (Grant No. 52088101), the National Natural Science Foundation of China (NSFC, Grant Nos. 11874409, 11804380, 11434014, 12074416, 51831012, and 51701203), the Beijing Natural Science Foundation (Grant No. Z190009), and partially supported by the Strategic Priority Research Program (B) (Grant No. XDB07030200), the Key Research Program of Frontier Sciences (Grant No. QYZDJ-SSW-SLH016), the International Partnership Program (Grant No. 112111KY5B20170090) of the Chinese Academy of Sciences (CAS), the Youth Innovation Promotion Association of CAS (Grant No. 2018008), the China Postdoctoral Science Foundation (Grant No. 2020M670499), and the K. C. Wong Education Foundation (Grant No. GJTD-2019-14). The authors also thank Prof. Wanjun Jiang, Dr. Hengan Zhou, and Dr. Teng Xu for their help in device fabrication and Prof. Zhijun Wang for fruitful discussions.

Conflict of Interest

The authors declare no conflict of interest.

Data Availability Statement

Data available on request from the authors.

Keywords

octahedral distortion, spin Hall conductivity, spin-orbit torque, spin-torque ferromagnetic resonance, SrRuO₃ films

Received: January 13, 2021

Revised: March 25, 2021

Published online:

- [1] I. M. Miron, K. Garello, G. Gaudin, P.-J. Zermatten, M. V. Costache, S. Auffret, S. Bandiera, B. Rodmacq, A. Schuhl, P. Gambardella, *Nature* **2011**, 476, 189.
- [2] L. Q. Liu, C.-F. Pai, D. C. Ralph, R. A. Buhrman, *Phys. Rev. Lett.* **2012**, 109, 186602.
- [3] G. Yu, P. Upadhyaya, Y. Fan, J. G. Alzate, W. Jiang, K. L. Wong, S. Takei, S. A. Bender, L.-T. Chang, Y. Jiang, M. Lang, J. Tang, Y. Wang, Y. Tserkovnyak, P. K. Amiri, K. L. Wang, *Nat. Nanotechnol.* **2014**, 9, 548.
- [4] C. Song, R. Zhang, L. Liao, Y. Zhou, X. Zhou, R. Chen, Y. You, X. Chen, F. Pan, *Prog. Mater. Sci.* **2021**, 118, 100761.
- [5] R. Mathieu, A. Asamitsu, H. Yamada, K. S. Takahashi, M. Kawasaki, Z. Fang, N. Nagaosa, Y. Tokura, *Phys. Rev. Lett.* **2004**, 93, 016602.
- [6] D. Xiao, M.-C. Chang, Q. Niu, *Rev. Mod. Phys.* **2010**, 82, 1959.
- [7] Y. F. Nie, P. D. C. King, C. H. Kim, M. Uchida, H. I. Wei, B. D. Faeth, J. P. Ruf, J. P. C. Ruff, L. Xie, X. Pan, C. J. Fennie, D. G. Schlom, K. M. Shen, *Phys. Rev. Lett.* **2015**, 114, 016401.
- [8] H. Kontani, T. Tanaka, D. S. Hirashima, K. Yamada, J. Inoue, *Phys. Rev. Lett.* **2008**, 100, 096601.
- [9] A. S. Patri, K. Hwang, H.-W. Lee, Y. B. Kim, *Sci. Rep.* **2018**, 8, 8052.
- [10] P. Jadauna, L. F. Registera, S. K. Banerjee, *Proc. Natl. Acad. Sci. USA* **2020**, 117, 11878.
- [11] G. Koster, L. Klein, W. Siemons, G. Rijnders, J. S. Dodge, C.-B. Eom, D. H. A. Blank, M. R. Beasley, *Rev. Mod. Phys.* **2012**, 84, 253.
- [12] M. W. Haverkort, I. S. Elfimov, L. H. Tjeng, G. A. Sawatzky, A. Damascelli, *Phys. Rev. Lett.* **2008**, 101, 026406.
- [13] M. Verissimo-Alves, P. García-Fernández, D. I. Bilc, P. Ghosez, J. Junquera, *Phys. Rev. Lett.* **2012**, 108, 107003.
- [14] L. Liu, Q. Qin, W. Lin, C. Li, Q. Xie, S. He, X. Shu, C. Zhou, Z. Lim, J. Yu, W. Lu, M. Li, X. Yan, S. J. Pennycook, J. Chen, *Nat. Nanotechnol.* **2019**, 14, 939.
- [15] J. Xia, Y. Maeno, P. T. Beyersdorf, M. M. Fejer, A. Kapitulnik, *Phys. Rev. Lett.* **2006**, 97, 167002.
- [16] P. Mahadevan, F. Aryasetiawan, A. Janotti, T. Sasaki, *Phys. Rev. B* **2009**, 80, 035106.
- [17] Q. Qin, L. Liu, W. Lin, X. Shu, Q. Xie, Z. Lim, C. Li, S. He, G. M. Chow, J. Chen, *Adv. Mater.* **2019**, 31, 1807008.
- [18] M. Wahler, N. Homonnay, T. Richter, A. Müller, C. Eischenschmidt, B. Fuhrmann, G. Schmidt, *Sci. Rep.* **2016**, 6, 28727.
- [19] T. Richter, M. Paleschke, M. Wahler, F. Heyroth, H. Deniz, D. Hesse, G. Schmidt, *Phys. Rev. B* **2017**, 96, 184407.
- [20] Y. Ou, Z. Wang, C. S. Chang, H. P. Nair, H. Paik, N. Reynolds, D. C. Ralph, D. A. Muller, D. G. Schlom, R. A. Buhrman, *Nano Lett.* **2019**, 19, 3663.
- [21] A. Vailionis, W. Siemons, G. Koster, *Appl. Phys. Lett.* **2008**, 93, 051909.
- [22] D. Kan, R. Aso, H. Kurata, Y. Shimakawa, *J. Appl. Phys.* **2013**, 113, 173912.
- [23] A. Vailionis, H. Boschker, W. Siemons, E. P. Houwman, D. H. A. Blank, G. Rijnders, G. Koster, *Phys. Rev. B* **2011**, 83, 064101.
- [24] W. Lu, W. Song, P. Yang, J. Ding, G. M. Chow, J. Chen, *Sci. Rep.* **2015**, 5, 10245.
- [25] A. J. Grutter, F. J. Wong, E. Arenholz, A. Vailionis, Y. Suzuki, *Phys. Rev. B* **2012**, 85, 134429.
- [26] A. T. Zayak, X. Huang, J. B. Neaton, K. M. Rabe, *Phys. Rev. B* **2006**, 74, 094104.
- [27] A. T. Zayak, X. Huang, J. B. Neaton, K. M. Rabe, *Phys. Rev. B* **2008**, 77, 214410.
- [28] L. Liu, T. Moriyama, D. C. Ralph, R. A. Buhrman, *Phys. Rev. Lett.* **2011**, 106, 036601.
- [29] A. R. Mellnik, J. S. Lee, A. Richardella, J. L. Grab, P. J. Mintum, M. H. Fischer, A. Vaezi, A. Manchon, E.-A. Kim, N. Samarth, D. C. Ralph, *Nature* **2014**, 511, 449.
- [30] C. He, G. Yu, C. Grezes, Z. Zhao, J. Feng, S. A. Razavi, Q. Shao, A. Navabi, X. Li, Q. L. He, M. Li, J. Zhang, K. L. Wong, D. Wei, G. Zhang, X. Han, P. K. Amiri, K. L. Wang, *Phys. Rev. Appl.* **2018**, 10, 034067.
- [31] J. Wei, C. He, X. Wang, H. Xu, Y. Liu, Y. Guang, C. Wan, J. Feng, G. Yu, X. Han, *Phys. Rev. Appl.* **2020**, 13, 034041.
- [32] C.-F. Pai, Y. Ou, L. H. Vilela-Leão, D. C. Ralph, R. A. Buhrman, *Phys. Rev. B* **2015**, 92, 064426.
- [33] Y. Ou, C.-F. Pai, S. Shi, D. C. Ralph, R. A. Buhrman, *Phys. Rev. B* **2016**, 94, 140414(R).
- [34] D. MacNeill, G. M. Stiehl, M. H. D. Guimaraes, R. A. Buhrman, J. Park, D. C. Ralph, *Nat. Phys.* **2017**, 13, 300.
- [35] J. Sklenar, W. Zhang, M. B. Jungfleisch, H. Saglam, S. Grudichak, W. Jiang, J. E. Pearson, J. B. Ketterson, A. Hoffmann, *Phys. Rev. B* **2017**, 95, 224431.
- [36] A. Okada, Y. Takeuchi, K. Furuya, C. Zhang, H. Sato, S. Fukami, H. Ohno, *Phys. Rev. Appl.* **2019**, 12, 014040.

- [37] T. Nan, T. J. Anderson, J. Gibbons, K. Hwang, N. Campbell, H. Zhou, Y. Q. Dong, G. Y. Kim, D. F. Shao, T. R. Paudel, N. Reynolds, X. J. Wang, N. X. Sun, E. Y. Tsybal, S. Y. Choi, M. S. Rzechowski, Yong Baek Kim, D. C. Ralph, C. B. Eom, *Proc. Natl. Acad. Sci. USA* **2019**, *116*, 16186.
- [38] W. Zhang, W. Han, X. Jiang, S.-H. Yang, S. S. P. Parkin, *Nat. Phys.* **2015**, *11*, 496.
- [39] M.-H. Nguyen, D. C. Ralph, R. A. Buhrman, *Phys. Rev. Lett.* **2016**, *116*, 126601.
- [40] L. Zhu, K. Sobotkiewich, X. Ma, X. Li, D. C. Ralph, R. A. Buhrman, *Adv. Funct. Mater.* **2019**, *29*, 1805822.
- [41] C.-F. Pai, L. Liu, Y. Li, H. W. Tseng, D. C. Ralph, R. A. Buhrman, *Appl. Phys. Lett.* **2012**, *101*, 122404.
- [42] Y.-C. Lau, M. Hayashi, *Jpn. J. Appl. Phys.* **2017**, *56*, 0802B5.
- [43] Q. Shao, C. Tang, G. Yu, A. Navabi, H. Wu, C. He, J. Li, P. Upadhyaya, P. Zhang, S. A. Razavi, Q. L. He, Y. Liu, P. Yang, S. K. Kim, C. Zheng, Y. Liu, L. Pan, R. K. Lake, X. Han, Y. Tserkovnyak, J. Shi, K. L. Wang, *Nat. Commun.* **2018**, *9*, 3612.
- [44] L. Zhu, D. C. Ralph, R. A. Buhrman, *Phys. Rev. Lett.* **2019**, *123*, 057203.
- [45] W. Lu, K. He, W. Song, C.-J. Sun, G. M. Chow, J.-S. Chen, *J. Appl. Phys.* **2013**, *113*, 17E125.